

 Very Important Paper


 Special Collection

Aerosol-Based Synthesis of Multi-metal Electrocatalysts for Oxygen Evolution and Glycerol Oxidation

Ieva A. Cechanaviciute,^[a] Tim Bobrowski,^[a] Daliborka Jambrec,^[a] Olga A. Krysiak,^[a] Ann Cathrin Brix,^[a] Michael Braun,^[b] Thomas Quast,^[a] Patrick Wilde,^[a] Dulce M. Morales,^[c] Corina Andronesu,^[b] and Wolfgang Schuhmann*^[a]

Discovery of new catalysts is crucial for future growth and development of environmentally friendly energy conversion processes e.g. the production of hydrogen by water electrolysis. We developed an aerosol-based synthesis technique as a comparatively fast and facile method to prepare multi-metal catalysts. 22 different quinary metal compositions were synthesized and investigated with respect to their activity for the oxygen evolution (OER) and the glycerol oxidation (GOR) reactions. The impact of the element composition and the homogeneous distribution of the elements in the particles on

catalytic performance were evaluated. The highest activity for OER was found for Co₂₀Cu₂₀Ni₂₀Fe₂₀Zn₂₀. For GOR, Ag-containing catalysts were the most active, however, in most cases Ag was locally enriched and not homogeneously mixed with the other metals in the particles. Ag-based catalysts outperformed similar compositions containing one or more noble metals. The GOR selectivity of selected catalysts during long-term electrolysis was also investigated and it was shown that varying the catalyst composition via aerosol-based synthesis is a potential way to modulate the GOR selectivity.

Introduction

“Green” energy production, conversion and storage includes various chemical reactions whose successful control via electrocatalytic processes is the key to enable them. For water electrolysis and specifically the more demanding oxygen evolution reaction (OER), noble metals such as Ru- and Ir-based catalysts exhibit benchmark activities especially in acidic electrolytes.^[1] However, constant efforts are made to develop new and improved materials that could replace or reduce the utilization of noble metals.

A feasible strategy to develop and investigate new types of materials is to increase the number of elements in the catalyst composition. The fundamental concept does not only include

the increase of the number of possible combinations and especially the variability of active sites exposed at the surface but also the possibility for synergistic effects between the individual constituting components. Multiple studies report considerable improvements in catalytic performance for various reactions by introducing a third component into binary metal structures.^[2,3] Especially the combination of multiple metals showed promising results for the OER.^[4] By increasing the complexity of the catalysts, among other properties, the electrical conductivity^[5] and stability may be modulated,^[6] electronic interactions between components may favorably influence the adsorption energies^[7] or create unique active sites due to synergistic interactions between the elements.^[8] A significant improvement of trimetallic catalysts over bimetallic compositions has been shown for the electrochemical alcohol oxidation, that can be employed as an alternative to the OER during water splitting.^[9]

Single-phase complex solid solutions (CSS), also known as high-entropy alloys (HEA), are another class of multi-component materials that are comprised of at least five elements in a near equiatomic composition and homogeneously distributed in a crystalline solid-solution phase.^[10] HEAs recently gained fast growing interest not only because of their unprecedented mechanical and physical properties but also due to their possible application as electrocatalysts e.g. for nitrogen reduction,^[11] ammonia decomposition^[12] or methanol oxidation.^[13] For the ORR noble metal-free Cr–Mn–Fe–Co–Ni nanoparticles synthesized by combinatorial co-sputtering into an ionic liquid were shown to reach catalytic activities comparable with Pt.^[14] Highly active OER catalysts with good electrochemical durability based on Al–Ni–Co–Fe–X (X=Mo, Nb, Cr) were reported as an example of how catalytic properties can be influenced by the changes in the materials composition.^[15] However, not only crystalline multi-component structures like

[a] I. A. Cechanaviciute, Dr. T. Bobrowski, Dr. D. Jambrec, Dr. O. A. Krysiak, A. C. Brix, T. Quast, Dr. P. Wilde, Prof. W. Schuhmann
Analytical Chemistry – Center for Electrochemical Sciences (CES), Faculty of Chemistry and Biochemistry
Ruhr University Bochum
Universitätsstr. 150, 44780 Bochum, Germany
E-mail: wolfgang.schuhmann@rub.de

[b] M. Braun, Prof. C. Andronesu
Chemical Technology III, Faculty of Chemistry and CENIDE - Center for Nanointegration
University of Duisburg-Essen
Carl-Benz-Straße 199, 47057 Duisburg, Germany

[c] Dr. D. M. Morales
Nachwuchsgruppe Gestaltung des Sauerstoffentwicklungsmechanismus
Helmholtz-Zentrum Berlin für Materialien und Energie GmbH
Hahn-Meitner-Platz 1, 14109 Berlin, Germany

 Supporting information for this article is available on the WWW under <https://doi.org/10.1002/celec.202200107>

 An invited contribution to the Hubert Girault Festschrift

 © 2022 The Authors. ChemElectroChem published by Wiley-VCH GmbH. This is an open access article under the terms of the Creative Commons Attribution Non-Commercial NoDerivs License, which permits use and distribution in any medium, provided the original work is properly cited, the use is non-commercial and no modifications or adaptations are made.

HEAs have been investigated as promising future catalysts. Engineering the local surface structure can also be realized by increasing the catalyst complexity to possibly create unique active sites and grain boundaries between different elements that are in close proximity. This was shown by *operando* ambient-pressure X-ray photoelectron spectroscopy and X-ray absorption spectroscopy measurements of (Ni–Fe–Co–Ce) O_x for the OER which revealed the influence of sharp grain boundaries between the separated CeO_2 phases and alloyed transition metal particles on the catalytic performance. The formation of active species such as Ni, Co and Fe oxyhydroxides occurred at a lower potential due to synergistic interactions with nanocrystalline CeO_2 boosting water oxidation kinetics.^[16] Evidently, multi-metal catalysts offer a huge research playground.

The only way to experimentally tackle the sheer number of different possible material combinations is to develop a synthesis method, which promises quick, easy and reliable catalyst formation. Moreover, a straightforward catalyst fabrication technique offers a major advantage compared to previously proposed and sometimes complicated synthesis routes such as carbothermal shock synthesis,^[17] laser ablation,^[18] spark plasma sintering^[19] or plasma arc discharge synthesis.^[20]

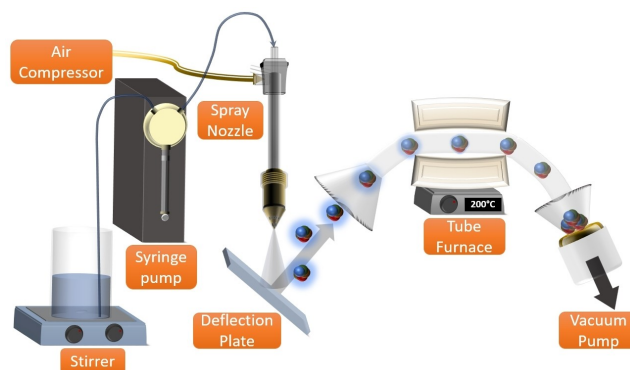
We developed an aerosol spraying technique which enables the simple and low-cost production of mixed-metal particles for a wide range of elements. As the presence of high entropy effect was not investigated, we refer to the obtained materials as multi-metal catalysts, although some of the compositions could essentially fit in into the class of high-entropy materials. We demonstrate the application of the obtained quinary metal composites as possible catalysts for the OER and the more complex glycerol oxidation reaction (GOR) and highlight the influence of composition and catalyst structure on the catalytic performance.

Results and Discussion

A spray-coating platform^[21] was modified and extended with a tube furnace and a vacuum pump to meet the requirements for the envisioned aerosol particle synthesis method (Scheme 1).

Briefly, a homogeneous metal salt solution with the target composition of the individual components is transported to the spray nozzle by a syringe pump and sprayed onto a deflector plate with the help of compressed air. This creates an aerosol, where each droplet supposedly contains the dissolved metal precursors in the previously set concentration. Subsequently, the droplets are passed through a tube, which can be heated with a tube furnace to remove the solvent. A vacuum pump connected to the outlet of the tube provides constant suction. As the aerosol travels through the tube, the solvent gradually evaporates, so that at the end small and dried particles of the catalyst precursors are collected on a filter paper.

In order to convert the precursor materials into multi-metal composites, the particles were transferred into a ceramic boat and subjected to a two-stage heating process. At first, residues of the filter paper were burned away at 700 °C in air which also led to the formation of the corresponding multi-metal oxides



Scheme 1. Aerosol-based synthesis technique to produce multi-metal catalysts. A constantly stirred metal precursor-containing solution is pumped to the spray nozzle and sprayed onto the deflection plate using compressed air to create an aerosol. With the help of a vacuum pump droplets are then sucked through the heated tube of a furnace (200 °C) to evaporate the solvent. The metal particles are finally caught in a filter paper and then further subjected to filter paper removal by oxidation followed by the reduction of the obtained materials in specific heating processes.

due to decomposition of the metal salts. Secondly, the multi-metal oxides underwent a reduction process at 400 °C in H_2/Ar (5%/95%) atmosphere to convert the catalysts into the desired reduced metallic form. Prior to electrochemical characterization, the obtained materials were studied using scanning transmission electron microscopy with energy-dispersive X-ray spectroscopy (STEM-EDS) (Figure 1).

The shown particle of a $CoCuFeMnZn$ composite shows a size of approximately 150 nm with all metals being homogeneously distributed in terms of random arrangement of elements across the whole particle. Inductively-coupled plasma mass spectrometry (ICP-MS) analysis data validated that in the resulting materials compositions the relative metal contents of the initial precursor mixture were retained, namely about ~20% for each metal. Using this synthesis approach, a total of 30 different catalysts were synthesized and their electrocatalytic properties for different oxidation reactions were evaluated. The elemental ratios are indicated according to the atomic metal

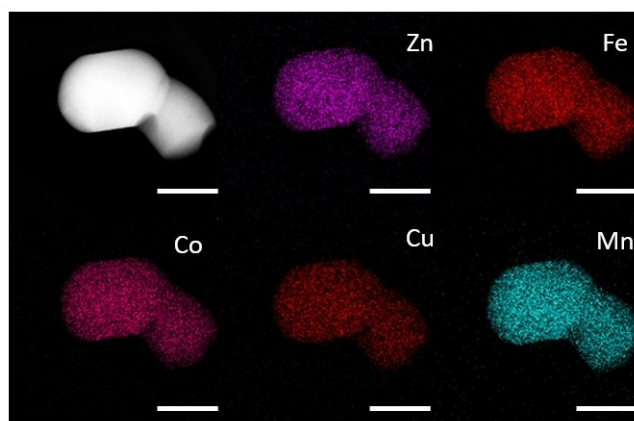


Figure 1. TEM-EDS mapping of a $CoCuFeMnZn$ particle in its oxidized form. The scale bar equals 100 nm.

ratio supplied in the initial spraying solution. For a consistent comparison of the electrocatalytic properties of the complex quinary compositions, it was decided to keep the composite partially fixed with the elements Co, Cu and Ni being in the majority of the compositions with the exception of one pure noble metal catalyst $\text{Ag}_{20}\text{Ir}_{20}\text{Pd}_{20}\text{Pt}_{20}\text{Ru}_{20}$. Aiming for a low number of different metallic phases inside the catalyst particles, Co, Cu and Ni were chosen as main components as they are compatible with respect to their enthalpies of formation of the lowest energy structure of each binary compound as shown by Troparevski *et al.*^[22] Moreover, Cu and Ni closely follow the Hume-Rothery rules for solid-solution formation^[23] with similar atomic radii and electronegativity values. Sufficiently good compatibility and miscibility between the elements are necessary to ensure the random elemental distribution and thus the formation of different active sites between neighboring metal atoms. In quinary compositions a huge variety of different active sites on the surface also creates a variety of unique, potentially highly active catalytic sites. Due to the simple catalyst synthesis and easily applied alterations of catalyst compositions using the proposed aerosol-based synthesis technique, it is feasible to synthesize a wide variety of composites in a relatively short time and evaluate their catalytic activity in relation to their elemental composition.

At first, catalyst screening for the OER was performed. OER was chosen as a model reaction due to its fundamental importance in electrocatalysis and its key role in water electrolysis. Due to the sluggish four-electron transfer process and high overpotential values necessary to initiate the OER, improved catalysts development is the key to the advancement of hydrogen evolution that acts as a counter reaction to the OER.^[24] As the electrocatalytic behavior was our primary interest during the catalyst screening procedure, a detailed structural analysis of the catalysts was performed later in the study.

Electrocatalytic activity towards the OER was evaluated in terms of current normalized by the geometric area of the electrode by performing rotating disk electrode (RDE) voltammetric measurements in 1 M KOH. The obtained current densities were compared at 1.7 V vs. RHE. A full list of catalysts investigated for OER is presented in Figure S1 and the voltammograms of the 9 best-performing catalyst obtained during the RDE measurements are presented in Figure 2. Based on the proposed OER four-step mechanism (cf. equations (1)–(4)) at alkaline conditions,^[25] there is consensus that an OER catalyst, oxygen-free materials acting as “pre-catalysts”, have to be converted into their corresponding oxides (3) or hydroxides (4) first,^[26] whereas the already oxidized forms do not have to undergo this step.

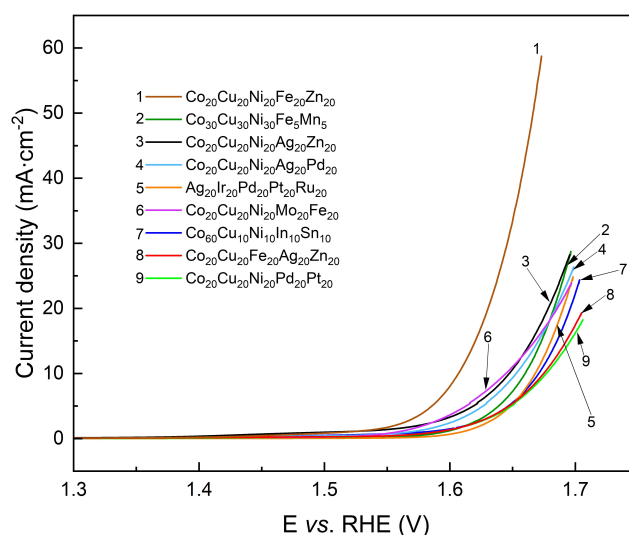
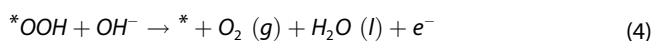


Figure 2. RDE voltammograms of 9 best performing OER catalyst compositions in terms of current density values. Voltammograms recorded from 1 to 1.7 V at 10 mV s^{-1} scanning rate in 1 M KOH solution at 1600 rpm. Catalyst list from the most active to the least active catalyst in terms of current density value at 1.7 V: 1 – $\text{Co}_{20}\text{Cu}_{20}\text{Ni}_{20}\text{Fe}_{20}\text{Zn}_{20}$, 2 – $\text{Co}_{30}\text{Cu}_{30}\text{Ni}_{30}\text{Fe}_3\text{Mn}_5$, 3 – $\text{Co}_{20}\text{Cu}_{20}\text{Ni}_{20}\text{Ag}_{20}\text{Zn}_{20}$, 4 – $\text{Co}_{20}\text{Cu}_{20}\text{Ni}_{20}\text{Ag}_{20}\text{Pd}_{20}$, 5 – $\text{Ag}_{20}\text{Ir}_{20}\text{Pd}_{20}\text{Pt}_{20}\text{Ru}_{20}$, 6 – $\text{Co}_{20}\text{Cu}_{20}\text{Ni}_{20}\text{Mo}_{20}\text{Fe}_{20}$, 7 – $\text{Co}_{60}\text{Cu}_{10}\text{Ni}_{10}\text{In}_{10}\text{Sn}_{10}$, 8 – $\text{Co}_{20}\text{Cu}_{20}\text{Fe}_{20}\text{Ag}_{20}\text{Zn}_{20}$, 9 – $\text{Co}_{20}\text{Cu}_{20}\text{Ni}_{20}\text{Pd}_{20}\text{Pt}_{20}$.

However, an oxygen-rich lattice can cause electrical conductivity problems in contrast to the active form of the catalyst obtained by electrochemical oxidation of potentially only a shell of the metal and hence may negatively affect the overall catalyst performance.

Moreover, all selected oxidized forms that were measured for the OER demonstrated lower catalytic activity in terms of current density than their corresponding reduced forms (Figure S2). Thus, only materials obtained after thermal reduction in H_2/Ar atmosphere were further investigated. This way, a better comparability between catalysts can be ensured than with the previously oxidized form with an undefined oxide/hydroxide layer. During OER measurements it was found that the catalytic activity is strongly affected by the variation of the elemental ratio. By varying the amount of Co, Cu, and Ni in the initial synthesis solution of different CoCuNiInSn samples, we observed that the recorded OER current density increases from 3 mA cm^{-2} for equimolar $\text{Co}_{20}\text{Cu}_{20}\text{Ni}_{20}\text{In}_{20}\text{Sn}_{20}$ to 23 mA cm^{-2} at 1.7 V vs. RHE when the Co concentration was increased to 60% ($\text{Co}_{60}\text{Cu}_{10}\text{Ni}_{10}\text{In}_{10}\text{Sn}_{10}$) (Figure S3). This rather unusual composition was chosen to investigate the influence of less conventional elements in the multi-metal catalysts. Out of all investigated composites, the highest catalytic activity towards the OER was obtained with $\text{Co}_{20}\text{Cu}_{20}\text{Ni}_{20}\text{Fe}_{20}\text{Zn}_{20}$ reaching total current density values of 58 mA cm^{-2} at 1.67 V vs. RHE, Figure 2, line 1). Even though the specific role of each element in enhancing the activity of the multi-metal catalysts has not been fully understood yet, a positive influence of Fe in combination with Co and Ni can be expected based on previous investigations.^[3,27] Multiple explanations have been presented and possible mechanisms proposed to rationalize the significant

improvement in catalytic activity when Fe is introduced into a bi-metallic CoNi structure.^[28] Moreover, other quinary compositions containing Co, Ni and Fe also showed high currents with $\text{Co}_{30}\text{Cu}_{30}\text{Ni}_{30}\text{Fe}_5\text{Mn}_5$ reaching 28 mA cm^{-2} (Figure 2, line 2) and thus exceeding the value of $\text{Ag}_{20}\text{Ir}_{20}\text{Pd}_{20}\text{Pt}_{20}\text{Ru}_{20}$, the only noble metal-containing catalyst investigated in this study, which only exhibited 24 mA cm^{-2} (Figure 2 line 5, Figure S1). A comparison with other OER electrocatalysts reported in the literature can be found in Table S1. For a better understanding of the catalyst structure and its influence on the performance, TEM-EDS analysis was performed for $\text{Co}_{20}\text{Cu}_{20}\text{Ni}_{20}\text{Fe}_{20}\text{Zn}_{20}$ (Figure 3) that demonstrated the highest activity towards OER in this study. EDS mapping displays uniform elemental distribution of Co, Ni, Fe, Cu and Zn, with the latter being visibly more concentrated in some areas than the other elements. According to ICP-MS, elements are distributed in nearly equiatomic composition in the range of 19–21% (Table 1). These findings support the formation of a random distribution of elements, which would allow the formation of different multi-metal active sites that might benefit from synergistic effects to enhance the electrocatalytic activity.

The high number of available materials and their applicability for electrochemical reaction such as the OER, led to the consideration that the obtained materials could also be employed for other multi-step oxidation reactions. Specifically, the oxidation of glycerol as an alternative to the OER as the anode reaction for clean hydrogen production is of great interest. Most multi-metal composites investigated for the OER contained Co, Cu and Ni that are known to be active for the catalytic conversion of glycerol.^[29,30,31] Glycerol, the main by-

product of biodiesel production, has attracted special attention because of its low price^[32] and potential for its conversion to value-added products due to the presence of three hydroxyl groups. Catalyst screening for the glycerol oxidation reaction (GOR) was performed in the presence of 0.1 M glycerol dissolved in 1 M KOH under the same conditions used for OER evaluation (Figure 4 and Figure S4). Due to a poor performance of the oxidized forms of the catalyst composites in terms of activity for the OER, only the reduced forms of the catalysts were investigated for the GOR. Catalytic activities obtained during the GOR with the different catalyst are compared at 1.5 V vs. RHE (Figure 5).

The highest catalytic activity towards glycerol oxidation out of all investigated materials was recorded for $\text{Co}_{20}\text{Cu}_{20}\text{Ni}_{20}\text{Ag}_{20}\text{Zn}_{20}$, reaching a current density of approximately 17 mA cm^{-2} at a potential value of 1.5 V vs. RHE. Interestingly, all the catalysts that performed well in terms of GOR activity contained Ni, which was not always the case for the OER. To overcome the competition between the GOR and the OER it is required that a GOR catalyst exhibits much lower overpotential value to initiate GOR compared to the OER (Figure S5). Due to the three available OH^- groups one molecule of glycerol could theoretically occupy up to three active surface sites and therefore be oxidized faster. At higher potentials competition between GOR and OER takes place and both reactions influence the shape of the voltammogram. In some cases, such as for noble metal-containing catalysts (line 19 in Figure S4, catalyst $\text{Ag}_{20}\text{Ir}_{20}\text{Pd}_{20}\text{Pt}_{20}\text{Ru}_{20}$) poisoning effects may occur based on the nature of the catalysts and the individual adsorption strength of the intermediates.

It is expected that an efficient GOR catalyst exhibits lower overpotentials to initiate the reaction than those required to

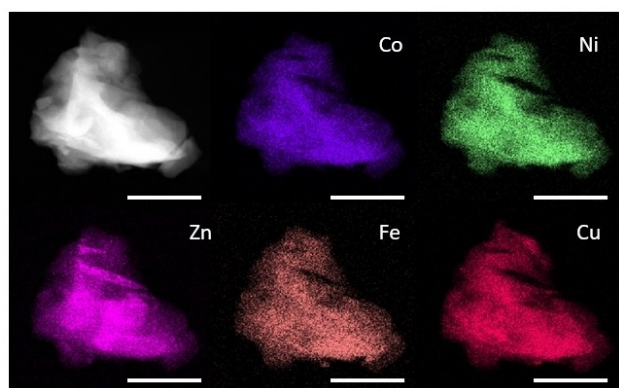


Figure 3. TEM-EDS mapping of a CoCuNiFeZn particle. The scale bar equals 100 nm

Table 1. Best-performing reduced forms of catalyst for OER and GOR.			
Reaction	Nominal elemental composition	Current density	Experimental data ICP-MS
OER	$\text{Co}_{20}\text{Cu}_{20}\text{Ni}_{20}\text{Fe}_{20}\text{Zn}_{20}$	58 mA cm^{-2} at 1.67 V vs. RHE	$\text{Co}_{19.9}\text{Cu}_{21.1}\text{Ni}_{19.2}\text{Fe}_{18.7}\text{Zn}_{21.1}$
GOR	$\text{Co}_{20}\text{Cu}_{20}\text{Ni}_{20}\text{Ag}_{20}\text{Zn}_{20}$	17 mA cm^{-2} at 1.5 V vs. RHE	$\text{Co}_{25.6}\text{Cu}_{20.2}\text{Ni}_{25.5}\text{Ag}_{4.0}\text{Zn}_{24.7}$

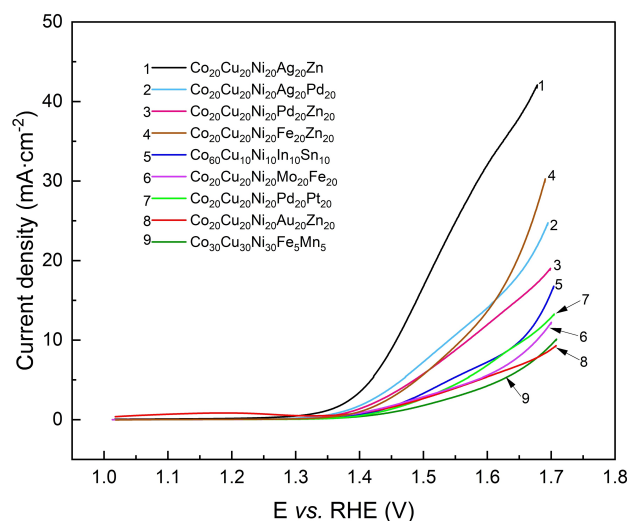


Figure 4. RDE voltammograms of 9 best performing GOR catalyst compositions in terms of current density values. Voltammograms recorded from 1 to 1.7 V at 10 mV s^{-1} scan rate in 1 M KOH solution at 1600 rpm. Catalyst list from the most active to the least active catalyst in terms of current density value at 1.7 V: 1 – $\text{Co}_{20}\text{Cu}_{20}\text{Ni}_{20}\text{Ag}_{20}\text{Zn}_{20}$, 2 – $\text{Co}_{20}\text{Cu}_{20}\text{Ni}_{20}\text{Ag}_{20}\text{Pd}_{20}$, 3 – $\text{Co}_{20}\text{Cu}_{20}\text{Ni}_{20}\text{Pd}_{20}\text{Zn}_{20}$, 4 – $\text{Co}_{20}\text{Cu}_{20}\text{Ni}_{20}\text{Fe}_{20}\text{Zn}_{20}$, 5 – $\text{Co}_{60}\text{Cu}_{10}\text{Ni}_{10}\text{In}_{10}\text{Sn}_{10}$, 6 – $\text{Co}_{20}\text{Cu}_{20}\text{Ni}_{20}\text{Mo}_{20}\text{Fe}_{20}$, 7 – $\text{Co}_{20}\text{Cu}_{20}\text{Ni}_{20}\text{Pd}_{20}\text{Pt}_{20}$, 8 – $\text{Co}_{20}\text{Cu}_{20}\text{Ni}_{20}\text{Au}_{20}\text{Zn}_{20}$, 9 – $\text{Co}_{30}\text{Cu}_{30}\text{Ni}_{30}\text{Fe}_5\text{Mn}_5$.

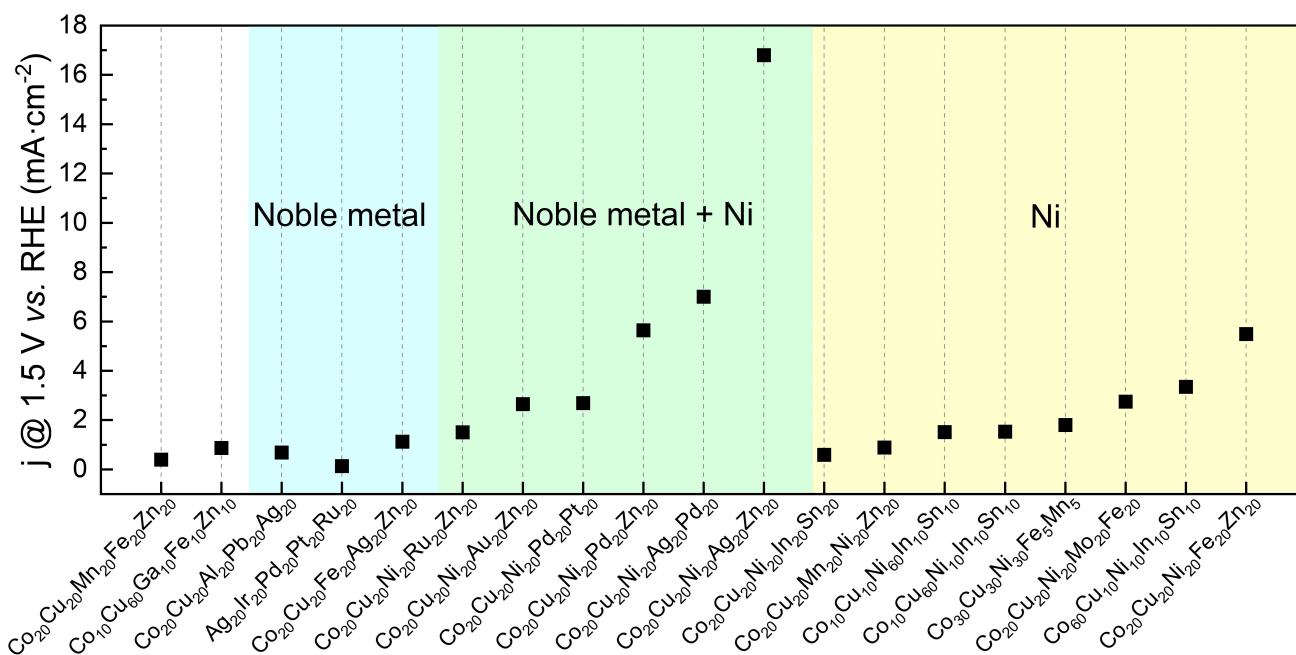


Figure 5. Catalytic performances of aerosol spray-synthesized multi-metal catalysts for GOR. Current densities at 1.5 V vs. RHE for GOR (■) are presented. Colours are used as a guideline for the eyes to highlight the catalyst groups that contain noble metals (■), both Ni and noble metal (■) and only Ni (■). Catalysts in the white region do not contain any of the aforementioned components.

initiate the OER in order to overcome the competition between the two reactions. In general, Ni-based catalysts have been reported to demonstrate comparatively lower overpotentials for the GOR than for the OER, with additional beneficial properties regarding the GOR selectivity.^[29,33] Furthermore, catalysts containing a small portion of noble metals show comparatively high activity. The presence of Ag in combinations like Co₂₀Cu₂₀Ni₂₀X₂₀Zn₂₀ beneficially affects current densities in comparison to other noble metals: XZ = PdPt (3 mA cm⁻²) < PdZn (6 mA cm⁻²) < PdAg (7 mA cm⁻²) < AgZn (17 mA cm⁻²) at 1.5 V vs. RHE. Catalysts containing Au and Ru (together with Co, Cu, Ni and Zn) displayed low current densities of approximately only 3 mA cm⁻² and 2 mA cm⁻² at 1.5 V vs. RHE, respectively (Figure S6). Similar behavior of Ag-based compounds has already been discussed in the literature before as it was reported that interaction between Ag and noble metals in bi- and tri-metallic compositions lead to substantial changes in the adsorption energies of the catalytically active species during alcohol oxidation.^[34] For example, together with Pd it is suggested that Ag either is an oxygen source for alcohol oxidation at lower potentials or that it alters the electronic properties of Pd thus yielding a more active catalytic surface.^[35] Moreover, because of electronic and bi-functional effects, Ag-containing composites also demonstrate higher tolerance with respect to poisoning effects of CO-like species that are known to cause a significant decrease in activity in noble metal catalysts during oxidation of organic compounds.^[36] Another advantage of Ag as catalyst material is that it is considerably cheaper than other noble metals commonly used in catalysis (e.g. Pt, Au, Ru) and only a small amount of it is necessary for the composite synthesis, thus lowering the production cost

even more. A comparison of the catalyst performance with other noble and non-noble metal catalysts from the literature can be found in Table S1. TEM-EDS imaging of Co₂₀Cu₂₀Ni₂₀Ag₂₀Zn₂₀ revealed a higher degree of separation between the elements compared to its Fe-containing analog with well distributed Co, Ni, Cu and Zn and only small clusters (~30–100 nm) of Ag (Figure 6). ICP-MS results agree with EDS measurements indicating that only 4% of Ag is present in the composite while the other elements are present with 22–26% (Table 1). Since this catalyst demonstrated higher activity towards glycerol oxidation (17 mA cm⁻² at 1.5 V vs. RHE) than the one where Ag is replaced with homogeneously distributed Fe (5 mA cm⁻²), it can be hypothesized that the activity is

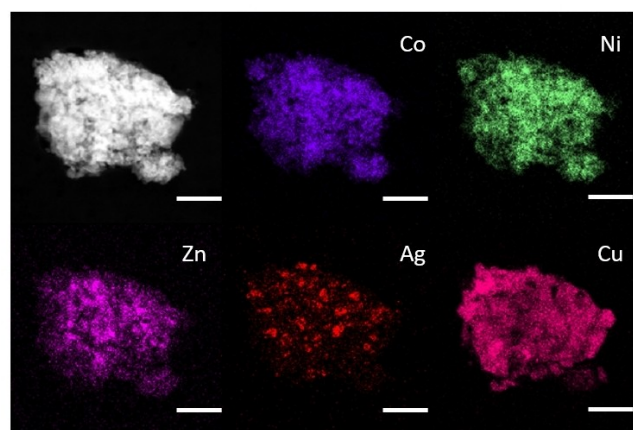


Figure 6. TEM-EDS mapping of a CoCuNiAgZn. The scale bars equal 300 nm.

positively influenced by the interface between the abundant Co, Cu, Ni, Zn and the small silver islands. However, it is important to mention that TEM-EDS cannot fully confirm the location of Ag, and other processes known to influence electrocatalytic activity like dealloying or strain effects could also play a role.^[37] Currently, only few studies on Ag/non-noble metal catalysts for alcohol oxidation are available.^[38]

Moreover, to the best of our knowledge no study has yet reported a tri-, tetra- or quinary-metallic Ag/transition metal catalyst composition for electrocatalytic oxidation of alcohols. To confirm that the behavior of $\text{Co}_{20}\text{Cu}_{20}\text{Ni}_{20}\text{Ag}_{20}\text{Zn}_{20}$ is indeed an effect of the interaction of the Ag islands with the “main” particle, additional RDE measurements were performed under the same conditions using Ag microparticles which were obtained via the aerosol-based synthesis. Only very low glycerol oxidation currents were registered during this control experiment. To further investigate how the Ag content influences the activity of the catalyst mixture, its content in the initial spraying solution was varied between 10 and 60%. It should be noted that at the same time the Ni content (as well as the content of the other elements) was changed accordingly. The following materials were synthesized and investigated: $\text{Co}_{10}\text{Cu}_{10}\text{Ni}_{60}\text{Ag}_{10}\text{Zn}_{10}$, $\text{Co}_{10}\text{Cu}_{10}\text{Ni}_{10}\text{Ag}_{60}\text{Zn}_{10}$ -red, and $\text{Co}_{22.5}\text{Cu}_{22.5}\text{Ni}_{22.5}\text{Ag}_{10}\text{Zn}_{22.5}$.

RDE voltammetry revealed no significant differences between measurements with an equimolar composition containing 20% Ag and the one where the Ag concentration is increased to 60% (Figure S7). Moreover, when $\text{Co}_{22.5}\text{Cu}_{22.5}\text{Ni}_{22.5}\text{Ag}_{10}\text{Zn}_{22.5}$ was used, the current density also remained similar at 1.5 V vs. RHE (22 mA cm^{-2}) and even surpassed that of other composites at higher potential values. On the other hand, notably lower current densities were observed for the catalyst where the initial Ni content was increased to 60%, while the content of Ag and other elements was lowered to 10%. When the Ag concentration was increased to 60%, the distribution of elements generally remained the same with the Ag clusters visible all over the nanoparticle (Figure S8). ICP-MS elemental analysis showed only 16% of Ag instead of the intended 60% provided in the spraying solution. Furthermore, for $\text{Co}_{22.5}\text{Cu}_{22.5}\text{Ni}_{22.5}\text{Ag}_{10}\text{Zn}_{22.5}$ and $\text{Co}_{10}\text{Cu}_{10}\text{Ni}_{60}\text{Ag}_{10}\text{Zn}_{10}$, the samples with 10% intended Ag content, only about 1% Ag was detected by ICP-MS (Table S2) and through TEM-EDS elemental mapping (Figure S9 and S10).

Although the presence of Ag was found to be important for the catalytic activity, fine-tuning of the amount of Ag had a rather small influence on the catalytic performance of the obtained CoCuNiAgZn compounds. RDE measurements and structural analysis could indicate the existence of energetic barriers, which lead to a poor miscibility of Ag within the metal matrix. However, it is also possible that a small fraction of Ag that is below the resolution of EDS could be intermixed with other elements due to the entropy effects. This would also explain the high catalytic activity for relatively low contents of Ag visible during glycerol oxidation. On the other hand, the variation of Ni, Co, Cu and Zn amounts yields clearer results possibly due to the good compatibility of these 3d transition metals. Even though a controlled variation of the catalyst

composition is desirable, it can also be observed that a high concentration of Ni affects catalytic activity negatively as in the comparison of the $\text{Co}_{22.5}\text{Cu}_{22.5}\text{Ni}_{22.5}\text{Ag}_{10}\text{Zn}_{22.5}$ and $\text{Co}_{10}\text{Cu}_{10}\text{Ni}_{60}\text{Ag}_{10}\text{Zn}_{10}$ samples. This emphasizes once more that not only the presence of specific elements but also the fine-tuning of their ratio is important for the overall catalytic performance.

Due to the multiple possible reaction pathways during the GOR, one of the biggest remaining challenges is to control or at least modulate product selectivity. The material with the highest activity, $\text{Co}_{20}\text{Cu}_{20}\text{Ni}_{20}\text{Ag}_{20}\text{Zn}_{20}$, was hence further studied. The ability of the catalyst to selectively form specific products was determined by performing glycerol electrolysis in a two-compartment flow-through cell (Figure S11).^[31] Measurements were performed at a constant potential of 1.5 V vs. RHE for 48 h while taking samples at fixed time intervals and subsequently performing product analysis using high-performance liquid chromatography (HPLC). For electrolysis, 0.1 M glycerol solution in 1 M KOH was used. However, to avoid further chemical transformation electrolysis samples are acidified converting the primarily formed organic acid salts into the corresponding acids that are detected during HPLC analysis. The main product during glycerol oxidation was formic acid, followed by oxalic acid and glycolic acid (Figure 7a). Additionally, traces of acetic, glyceric, and lactic acid were also observed (Figure 7b). The amount of formic, oxalic and acetic acid increased gradually throughout the measurement, while the concentration of glycolic, lactic, and glyceric acid reached a peak after a certain time, before their concentrations started to decrease presumably due to further oxidation. Almost half of the glycerol was converted during the first 24 h (47%). After that point, the conversion rate of glycerol slowed down, possibly also influenced by competing oxidation reactions of intermediates as it was e.g. observed for glycolic acid. After 48 h, about 66% of glycerol was converted. The catalyst $\text{Co}_{20}\text{Cu}_{20}\text{Ni}_{20}\text{Ag}_{20}\text{Zn}_{20}$ demonstrated high selectivity towards formic acid that reached almost 70% after 48 h. Formic acid is a higher value product than glycerol that is often applied as a preservative and antibacterial agent in livestock feed, a component in cleaning products or used for a leather and textile processing.^[39] Due to the rapid electrooxidation and low toxicity, formic acid is also an important compound for alternative energy production as it can be used as a fuel for direct formic acid fuel cells.^[40] The tendency of Ag to favor C_1 product formation is in agreement with previous research that employed Ag-containing catalysts.^[41] Wang and coworkers argued that a high production of formate is “Ag-like behavior” and demonstrated that increasing the amount of Ag on the catalyst surface drives the product selectivity towards formic acid.^[42] These findings were also confirmed by the observations made when $\text{Co}_{20}\text{Cu}_{20}\text{Ni}_{20}\text{Fe}_{20}\text{Zn}_{20}$ was used as catalyst during glycerol electrolysis (Figure S12). The selectivity towards formic acid formation dropped significantly in this case from 68% to 37%. Moreover, the concentration of acetic acid increased more than four times making it the compound with the second highest concentration after formic acid. Thus, the modification of the catalyst composition can be further explored in order to

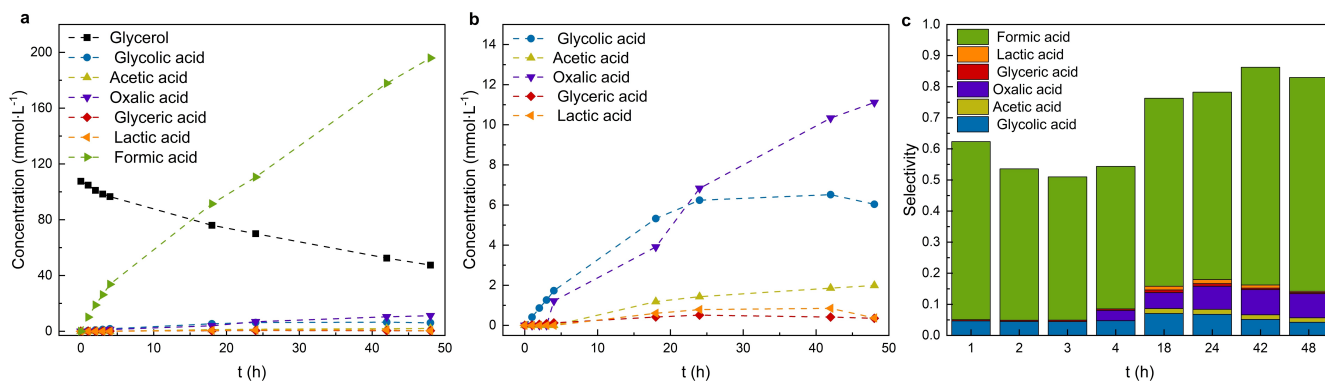


Figure 7. Glycerol oxidation measurement using $\text{Co}_{20}\text{Cu}_{20}\text{Ni}_{20}\text{Ag}_{20}\text{Zn}_{20}$ as a catalyst in 0.1 M glycerol in 1 M KOH and product analysis with HPLC. Concentration profiles during 48 h electrolysis: a) overview of glycerol and products, b) close-up excluding glycerol and formic acid, and c) selectivity as a fraction towards specific product formation. Dashed lines are a guide for the eyes.

achieve variations in product selectivity during glycerol oxidation.

Conclusion

In this work, we propose a new aerosol-based synthesis technique to produce multi-metal composites directly from a metal precursor solution. Using this method in total 22 different quinary materials compositions were obtained and investigated for their applicability for the OER as well as for the GOR. The influence of the elemental ratio and composition variation on catalytic activity was investigated. The highest catalytic activity towards OER in terms of current density at a set overpotential was exhibited by $\text{Co}_{20}\text{Cu}_{20}\text{Ni}_{20}\text{Fe}_{20}\text{Zn}_{20}$ with a current density of about 58 mA cm^{-2} at 1.7 V vs. RHE. During glycerol oxidation Ag plays a crucial role in increasing catalytic activity. Measurements with varying elemental ratios in CoCuNiAgZn revealed that even very low amounts of Ag (1%) led to a significant increase in current density. Even though Ag is not well miscible with other elements it is by far more beneficial for the selectivity and activity during GOR than well-distributed Ni. The selectivity of $\text{Co}_{20}\text{Cu}_{20}\text{Ni}_{20}\text{Ag}_{20}\text{Zn}_{20}$ for GOR was evaluated by performing glycerol electrolysis in a two-compartment flow-through cell which showed a glycerol conversion value of 66% in 48 h alongside a 68% selectivity towards the formation of formic acid.

Experimental Section

If not stated otherwise, nitrate forms of metal precursors were used for the aerosol-based synthesis route. For the synthesis of Ru-, Ir-, Sn-, Ir-containing catalysts, chloride precursors were used. Manganese (II) acetate tetrahydrate ($\text{C}_4\text{H}_6\text{MnO}_4 \times 4\text{H}_2\text{O}$) was used to obtain Mn, chloroauric acid (HAuCl_4) for Au composites and molybdenum (VI) oxide bis(2,4-pentanedionate) ($\text{C}_{10}\text{H}_{16}\text{MoO}_6$) for Mo. Co, Zn, Fe, Ni, Ag, Pd, Pt, Ru, Ga, In, Ir, Mn and Au precursors were purchased from Sigma-Aldrich and Cu, Al, Pb, Sn, Mo precursors from Alfa Aesar. All compounds were synthesis grade (98% or above). As electrolyte 1 M KOH (86.4%, Fisher Scientific) solution in ultra-pure water was used after purification with a Chelex 100 cation-

exchange resin (Sigma-Aldrich). For the preparation of glycerol solution, 0.1 M glycerol (99.9%, Fisher Scientific) was mixed in with 1 M KOH.

Electrochemical catalyst screening measurements were carried out using a rotating disk electrode comprising a RDE80983 rotator with a potentiostat/galvanostat Autolab PGSTAT 204 (Metrohm). Glassy carbon RDEs with a geometric area of 0.113 cm^2 , modified with the corresponding catalyst suspension, were used as working electrode. A self-made $\text{Ag}|\text{AgCl}|\text{KCl}$ (3 M) electrode with double junction (1 M KOH) was used as reference electrode and a Pt mesh was used as counter electrode. A glass compartment with a ceramic frit filled with electrolyte was used to separate the counter electrode from the bulk solution. For the electrode modification, 5 mg mL^{-1} catalyst was dispersed in a mixture consisting of equal volume parts of distilled water, ethanol and 2 vol% Nafion (49:49:2). The suspension was sonicated with a tip sonicator (Bandelin Sonopuls UW 3100) for 1 min (amplitude 25%, pulse duration 1 s) prior to use. The glassy carbon electrodes were polished using different roughness of polishing sheets: $3 \mu\text{m}$, $1 \mu\text{m}$, $0.3 \mu\text{m}$, and rinsed with distilled water before the catalyst deposition. For this, $4.8 \mu\text{L}$ of prepared suspension was drop-cast onto the polished working electrode surface, aiming for a nominal catalyst loading of approximately $210 \mu\text{g cm}^2$ and left to dry in air prior to measuring for at least 20 min. A conditioning procedure was conducted in 1 M KOH by potential cycling between 0 and 0.4 V vs. $\text{Ag}|\text{AgCl}|\text{KCl}$ (3 M) at 100 mV s^{-1} for 10 cycles. The RDE rotator speed during conditioning and other voltammetry measurements was kept constant at 1600 rpm. The catalytic activity for OER was evaluated by performing cyclic voltammetry measurements from 0 to 0.7 V vs. $\text{Ag}|\text{AgCl}|\text{KCl}$ (3 M) at 10 mV s^{-1} in 1 M KOH solution. The same CV procedure was also repeated in an electrolyte containing 0.1 M glycerol solution to observe the catalytic activity towards glycerol oxidation. Both solutions were purged with Ar (Air Liquide, Ar $\geq 99,999\%$) for at least 15 min and an Ar flow was maintained near the surface of the electrolyte throughout the measurements. All RDE measurements were repeated at least three times to ensure reproducibility (Figure S13). To compare catalytic activity between different catalysts the average current density value of a first forward scan at the certain potential was chosen. Current density was calculated based on the geometric area of the glassy carbon working electrode (5).

$$j = \frac{i \text{ (mA)}}{A \text{ (cm}^2\text{)}} \quad (5)$$

To determine the uncompensated resistance, electrochemical impedance spectra (EIS) were recorded after both CV measurements at open circuit potential (OPC), in a frequency range between 100 kHz and 10 Hz and an AC amplitude of 10 mV root mean squared (RMS) with no electrode rotation. Potentials recorded vs. Ag|AgCl|KCl (3 M) are converted to the reversible hydrogen electrode (RHE) by correcting the measured potential with the uncompensated resistance (R_u) obtained from Nyquist plots during EIS measurements and adding the formal potential of the reference electrode according to equation (6). The pH value was obtained considering the concentration of hydroxide in the electrolyte using the literature value of 0.766 for the activity of water (γ) (7).

$$E = E_{\text{measured}} - R_u \cdot i + E_{0,\text{Ag}/\text{AgCl}/\text{KCl}} + 0.059 \text{ pH} \quad (6)$$

$$\text{pH} = 14 + \log [\text{OH}^-] + \log(\gamma) \quad (7)$$

The selectivity of the catalyst was evaluated using a two-compartment flow-through cell, where the working electrode and the counter electrode compartments were separated using an anion-exchange membrane (Fumatech fumasep FAA-3-PK-130), which was soaked in 1 M KOH prior to use. 0.1 M glycerol solution in 1 M KOH was used for the circulation through the working electrode compartment and 1 M KOH was used for the counter electrode compartment. A home-made Ag|AgCl|KCl (3 M) electrode with double junction filled with 1 M KOH was used as the reference electrode. Ni foam (Goodfellow) was used as counter electrode and carbon paper (H23C2, Freudenberg) modified with the catalyst suspension acted as working electrode. 1.96 mg of catalyst was mixed with a solution of 98 vol% absolute ethanol and 2 vol% Nafion to make a suspension, which was deposited onto the surface of carbon paper via drop-casting, to achieve a loading of 1 mg cm² and left to dry overnight. After the cell was assembled, the electrolyte was circulated for 15 min prior to the measurement. Then OCP was recorded for 1 min, EIS measurements were conducted galvanostatically at a current of 0 A in the frequency range from 100 to 1 kHz with 50 μ A AC perturbation amplitude (RMS) followed by a CV between 0 and 0.5 V vs. Ag|AgCl|KCl (3 M) at a scan rate of 10 mV s⁻¹. Subsequently, a LSV was recorded between 0 and 0.5 V vs. Ag|AgCl|KCl (3 M) and the final potential was held for 48 h. Electrochemical measurements were carried out using a VSP-300 potentiostat (BioLogic) controlled by the EC Lab software. 350 μ L liquid samples were taken before chronoamperometry and after 1 h, 2 h, 3 h, 4 h, 16 h, 24 h, 42 h, and 48 h. To avoid further chemical transformation of unstable intermediates, samples were acidified with 530 mM HPLC grade H₂SO₄ (Merck, 98%) solution. The mixture was subsequently filtered with a 0.2 μ m syringe filter to remove any particles before HPLC analysis. Selectivity was calculated according to the Equation (8), where n_p is the amount of product and n_k is the amount of reactant (glycerol) in moles at a certain time of electrolysis compared to their initial amounts $n_{p,0}$ and $n_{k,0}$. Stoichiometry factor for glycerol (ν_k) = 1, and ν_p (C₁ products) = 3, ν_p (C₂ products) = 1.5, ν_p (C₃ products) = 1.

$$S_p = \frac{n_p - n_{p,0}}{n_{k,0} - n_k} \frac{|\nu_k|}{\nu_p} \quad (8)$$

Product analysis was carried out using high-performance liquid chromatography (HPLC) with the Dionex ICS-5000+ system (ThermoFischer) equipped with a refractive index (RI) detector (Knauer RefractoMax520), a diode array detector (Dionex UltiMate 3000) and an ion-exclusion column and precolumn (Bio-Rad Aminex HPX-87H). To enable product separation, the column compartment was heated to 70 °C and 4 mM H₂SO₄ was used as eluent with a flow rate of 0.6 mL min⁻¹. STEM was performed on a JEM-2800

(JEOL) with a Schottky-type field emission gun working at 200 kV with a point-to-point resolution of 0.20 nm and 0.14 nm. The spherical aberration and the chromatic aberration are 0.7 mm and 1.3 mm, respectively. EDS mapping was performed with the equipped double SDD detectors, with a solid angle of 0.98 sr with a detection area of 100 mm². Samples were typically prepared by drop-casting of catalyst ink onto a carbon film-coated copper or gold mesh. Elemental ratios in the catalysts were determined with ICP-MS (Anton Paar Multiwave PRO) after adding 4 mL of concentrated nitric acid to approximately 1 mg of sample and filling up to 10 mL with water. The average ppb values for Ni-60, Cu-63, Zn-66, Ag-107, Mn-55, Fe-57, Co-59 isotopes from 5 runs were divided by the weighed-in mass thus obtaining the element content in the sample.

Author Contributions

Ieva A. Cechanavičiute: investigation – electrochemical RDE measurements, flow-through cell selectivity measurements, visualization, writing – original draft preparation. Tim Bobrowski: investigation – development of the aerosol-based synthesis technique, multi-metal catalyst synthesis, visualization, writing – original draft preparation. Daliborka Jambreć: formal analysis, supervision. Olga A. Krysiak: investigation – multi-metal catalyst synthesis. Ann Cathrin Brix: investigation – RDE measurements. Michael Braun: investigation – HPLC analysis. Thomas Quast and Patrick Wilde: investigation – catalyst characterization (TEM-EDS). Dulce M. Morales: conceptualization, writing – review and editing. Corina Andronescu: supervision, writing – review and editing. Wolfgang Schuhmann: conceptualization, resources, supervision, writing – review and editing, project administration.

Acknowledgements

The Deutsche Forschungsgemeinschaft is acknowledged for funding in the framework of the Research Unit 2982 “UNODE – Unusual Anode Reactions” [433304666, 433304702]. This work is supported by the “Center for Solvation Science ZEMOS” funded by the German Federal Ministry of Education and Research BMBF and by the Ministry of Culture and Research of North Rhine-Westphalia. The authors acknowledge the contribution of Martin Trautmann for performing ICP-MS measurements, and João R. C. Junqueira for the initial design of the flow-through electrolyzer. Open Access funding enabled and organized by Projekt DEAL.

Conflict of Interest

The authors declare no conflict of interest.

Data Availability Statement

The data that support the findings of this study are available from the corresponding author upon reasonable request.

Keywords: Aerosol-based synthesis · Electrocatalysis · Glycerol oxidation · Multi-metal catalysts · Oxygen evolution

- [1] a) C. C. L. McCrory, S. Jung, J. C. Peters, T. F. Jaramillo, *J. Am. Chem. Soc.* **2013**, *135*, 16977–16987; b) Y. Lee, J. Suntivich, K. J. May, E. E. Perry, Y. Shao-Horn, *J. Phys. Chem. Lett.* **2012**, *3*, 399–404.
- [2] G. Sharma, D. Kumar, A. Kumar, A. H. Al-Muhtaseb, D. Pathania, M. Naushad, G. T. Mola, *Mater. Sci. Eng. C* **2017**, *71*, 1216–1230.
- [3] M. Khalid, A. M. B. Honorato, G. Tremiliosi Filho, H. Varela, *J. Mater. Chem. A* **2020**, *8*, 9021–9031.
- [4] J.-Y. Xue, C. Li, F.-L. Li, H.-W. Gu, P. Braunstein, J.-P. Lang, *Nanoscale* **2020**, *12*, 4816–4825.
- [5] a) Q. Qian, Y. Li, Y. Liu, L. Yu, G. Zhang, *Adv. Mater.* **2019**, *31*, e1901139; b) J.-Q. Chi, K.-L. Yan, Z. Xiao, B. Dong, X. Shang, W.-K. Gao, X. Li, Y.-M. Chai, C.-G. Liu, *Int. J. Hydrogen Energy* **2017**, *42*, 20599–20607; c) B. Liu, M. Zhang, Y. Wang, Z. Chen, K. Yan, *J. Alloys Compd.* **2021**, *852*, 156949.
- [6] M. A. Kazakova, D. M. Morales, C. Andronescu, K. Elumeeva, A. G. Selyutin, A. V. Ishchenko, G. V. Golubtsov, S. Dieckhöfer, W. Schuhmann, J. Masa, *Catal. Today* **2020**, *357*, 259–268.
- [7] a) A. Füngrlings, A. Koul, M. Dreyer, A. Rabe, D. M. Morales, W. Schuhmann, M. Behrens, R. Pentcheva, *Chem. Eur. J.* **2021**, *27*, 17145–17158; b) D. M. Morales, M. A. Kazakova, S. Dieckhöfer, A. G. Selyutin, G. V. Golubtsov, W. Schuhmann, J. Masa, *Adv. Funct. Mater.* **2020**, *30*, 1905992; c) R. Rajendiran, D. Chinnadurai, K. Chen, A. R. Selvaraj, K. Prabakar, O. L. Li, *ChemSusChem* **2021**, *14*, 1324–1335.
- [8] a) D. Senthil Raja, C.-L. Huang, Y.-A. Chen, Y. Choi, S.-Y. Lu, *Appl. Catal. B* **2020**, *279*, 119375; b) J. Jiang, F. Sun, S. Zhou, W. Hu, H. Zhang, J. Dong, Z. Jiang, J. Zhao, J. Li, W. Yan, M. Wang, *Nat. Commun.* **2018**, *9*, 2885.
- [9] a) K. Jiang, L. Bu, P. Wang, S. Guo, X. Huang, *ACS Appl. Mater. Interfaces* **2015**, *7*, 15061–15067; b) Z. Han, A.-J. Wang, L. Zhang, Z.-G. Wang, K.-M. Fang, Z.-Z. Yin, J.-J. Feng, *J. Colloid Interface Sci.* **2019**, *554*, 512–519; c) H. Lv, L. Sun, D. Xu, S. L. Suib, B. Liu, *Green Chem.* **2019**, *21*, 2367–2374; d) H. Xu, J. Wang, B. Yan, S. Li, C. Wang, Y. Shiraishi, P. Yang, Y. Du, *Nanoscale* **2017**, *9*, 17004–17012.
- [10] a) B. Cantor, I. Chang, P. Knight, A. Vincent, *Mater. Sci. Eng. A* **2004**, *375–377*, 213–218; b) T. K. Chen, T. T. Shun, J. W. Yeh, M. S. Wong, *Surf. Coat. Technol.* **2004**, *188–189*, 193–200.
- [11] D. Zhang, H. Zhao, X. Wu, Y. Deng, Z. Wang, Y. Han, H. Li, Y. Shi, X. Chen, S. Li, J. Lai, B. Huang, L. Wang, *Adv. Funct. Mater.* **2021**, *31*, 2006939.
- [12] P. Xie, Y. Yao, Z. Huang, Z. Liu, J. Zhang, T. Li, G. Wang, R. Shahbazian-Yassar, L. Hu, C. Wang, *Nat. Commun.* **2019**, *10*, 4011.
- [13] A.-L. Wang, H.-C. Wan, H. Xu, Y.-X. Tong, G.-R. Li, *Electrochim. Acta* **2014**, *127*, 448–453.
- [14] a) T. Löffler, A. Ludwig, J. Rossmel, W. Schuhmann, *Angew. Chem. Int. Ed.* **2021**, *60*, 26894–26903; b) T. Löffler, H. Meyer, A. Savan, P. Wilde, A. Garzón Manjón, Y.-T. Chen, E. Ventosa, C. Scheu, A. Ludwig, W. Schuhmann, *Adv. Energy Mater.* **2018**, *8*, 1802269.
- [15] H.-J. Qiu, G. Fang, J. Gao, Y. Wen, J. Lv, H. Li, G. Xie, X. Liu, S. Sun, *ACS Materials Lett.* **2019**, *1*, 526–533.
- [16] a) M. Favaro, W. S. Drisdell, M. A. Marcus, J. M. Gregoire, E. J. Crumlin, J. A. Haber, J. Yano, *ACS Catal.* **2017**, *7*, 1248–1258; b) J. A. Haber, Y. Cai, S. Jung, C. Xiang, S. Mitrovic, J. Jin, A. T. Bell, J. M. Gregoire, *Energy Environ. Sci.* **2014**, *7*, 682–688.
- [17] Y. Yao, Z. Huang, P. Xie, S. D. Lacey, R. J. Jacob, H. Xie, F. Chen, A. Nie, T. Pu, M. Rehwoldt, D. Yu, M. R. Zachariah, C. Wang, R. Shahbazian-Yassar, J. Li, L. Hu, *Science* **2018**, *359*, 1489–1494.
- [18] a) F. Waag, Y. Li, A. R. Zieffuß, E. Bertin, M. Kamp, V. Duppel, G. Marzun, L. Kienle, S. Barcikowski, B. Gökce, *RSC Adv.* **2019**, *9*, 18547–18558; b) D. Redka, C. Gadelmeier, J. Winter, M. Spellauge, C. Eulenkamp, P. Calta, U. Glatzel, J. Minár, H. P. Huber, *Appl. Surf. Sci.* **2021**, *544*, 148839.
- [19] X. Yan, X. Zhang, F. Wang, T. Stockdale, Y. Dzenis, M. Nastasi, B. Cui, *JOM* **2019**, *71*, 2856–2867.
- [20] A. Mao, H. Xiang, X. Ran, Y. Li, X. Jin, H. Yu, X. Gu, *J. Alloys Compd.* **2019**, *775*, 1177–1183.
- [21] T. Bobrowski, F. Conzuelo, A. Ruff, V. Hartmann, A. Frank, T. Erichsen, M. M. Nowaczyk, W. Schuhmann, *ChemPlusChem* **2020**, *85*, 1396–1400.
- [22] M. C. Troparevsky, J. R. Morris, M. Daene, Y. Wang, A. R. Lupini, G. M. Stocks, *JOM* **2015**, *67*, 2350–2363.
- [23] W. Hume-Rothery, H. M. Powell, *Z. Kristallogr.* **1935**, *91*, 23–47.
- [24] S. Wang, A. Lu, C.-J. Zhong, *Nano Convergence* **2021**, *8*, 4.
- [25] a) K. Zeng, D. Zhang, *Prog. Energy Combust. Sci.* **2010**, *36*, 307–326; b) H. Wendt, G. Imarisio, *J. Appl. Electrochem.* **1988**, *18*, 1–14.
- [26] a) X. Xu, F. Song, X. Hu, *Nat. Commun.* **2016**, *7*, 12324; b) Z. Kou, Y. Yu, X. Liu, X. Gao, L. Zheng, H. Zou, Y. Pang, Z. Wang, Z. Pan, J. He, S. J. Pennycook, J. Wang, *ACS Catal.* **2020**, *10*, 4411–4419; c) R. Li, B. Hu, T. Yu, H. Chen, Y. Wang, S. Song, *Adv. Sci.* **2020**, *7*, 1902830.
- [27] a) Z. Cao, Z. Jiang, Y. Li, C. Huang, Y. Li, *ChemSusChem* **2019**, *12*, 2480–2486; b) F.-T. Tsai, Y.-T. Deng, C.-W. Pao, J.-L. Chen, J.-F. Lee, K.-T. Lai, W.-F. Liaw, *J. Mater. Chem. A* **2020**, *8*, 9939–9950.
- [28] S. Anantharaj, S. Kundu, S. Noda, *Nano Energy* **2021**, *80*, 105514.
- [29] a) D. M. Morales, D. Jambrec, M. A. Kazakova, M. Braun, N. Sikdar, A. Koul, A. C. Brix, S. Seisel, C. Andronescu, W. Schuhmann, *ACS Catal.* **2022**, *12*, 982–992; b) V. L. Oliveira, C. Morais, K. Servat, T. W. Napporn, G. Tremiliosi-Filho, K. B. Kokoh, *Electrochim. Acta* **2014**, *117*, 255–262.
- [30] a) B. Habibi, N. Delnavaz, *RSC Adv.* **2016**, *6*, 31797–31806; b) V. L. Oliveira, C. Morais, K. Servat, T. W. Napporn, G. Tremiliosi-Filho, K. B. Kokoh, *Electrochim. Acta* **2014**, *117*, 255–262; c) M. R. Rizk, M. G. Abd El-Moghny, A. Mazhar, M. S. El-Deab, B. E. El-Anadoul, *Sustain. Energy Fuels* **2021**, *5*, 986–994.
- [31] A. C. Brix, D. M. Morales, M. Braun, D. Jambrec, J. R. C. Junqueira, S. Cychy, S. Seisel, J. Masa, M. Muhler, C. Andronescu, W. Schuhmann, *ChemElectroChem* **2021**, *8*, 2336–2342.
- [32] R. Ciriminna, C. Della Pina, M. Rossi, M. Pagliaro, *Eur. J. Lipid Sci. Technol.* **2014**, *116*, 1432–1439.
- [33] a) Q. Shao, J. Song, Y. Feng, X. Zhu, X. Huang, *ChemCatChem* **2018**, *10*, 3647–3652; b) Y. Li, X. Wei, L. Chen, J. Shi, M. He, *Nat. Commun.* **2019**, *10*, 5335.
- [34] a) A. C. Garcia, J. Caliman, E. B. Ferreira, G. Tremiliosi-Filho, J. J. Linares, *ChemElectroChem* **2015**, *2*, 1036–1041; b) J. B. Costa Santos, C. Vieira, R. Crisafulli, J. J. Linares, *Int. J. Hydrogen Energy* **2020**, *45*, 25658–25671.
- [35] Y. Holade, C. Morais, S. Arrii-Clacens, K. Servat, T. W. Napporn, K. B. Kokoh, *Electrocatalysis* **2013**, *4*, 167–178.
- [36] B. T. X. Lam, M. Chiku, E. Higuchi, H. Inoue, *J. Power Sources* **2015**, *297*, 149–157.
- [37] a) Y. Zhou, Y. Shen, J. Piao, *ChemElectroChem* **2018**, *5*, 1636; b) T. Bligaard, J. K. Nørskov, *Electrochim. Acta* **2007**, *18*, 5512–5516; Lai-Ming Luo, Wei Zhan, Rong-Hua Zhang, Qing-Yun Hu, Yi-Fei Guo, Xin-Wen Zhou, *J. Catal.* **2020**, *381*, 316–328.
- [38] a) E. A. Şahin, R. Solmaz, *Int. J. Hydrogen Energy* **2020**, *45*, 35013–35022; b) A. Ashok, A. Kumar, *Int. J. Hydrogen Energy* **2021**, *46*, 4788–4797.
- [39] BASF, “Formic Acid | CAS No. 64–18–6 |”, to be found under <https://products.basf.com/global/en/ci/formic-acid.html>, **2021**.
- [40] C. Ricea, S. Ha, R. I. Masel, P. Waszczuk, A. Wieckowski, Tom Barnard, *J. Power Sources* **2002**, *111*, 83–89.
- [41] J. F. Gomes, A. C. Garcia, L. Gasparotto, N. E. de Souza, E. B. Ferreira, C. Pires, G. Tremiliosi-Filho, *Electrochim. Acta* **2014**, *144*, 361–368.
- [42] L. Thia, M. Xie, D. Kim, X. Wang, *Catal. Sci. Technol.* **2017**, *7*, 874–881.

Manuscript received: January 28, 2022

Revised manuscript received: April 9, 2022

Accepted manuscript online: April 13, 2022